arXiv:1803.03441v1 [nlin.PS] 9 Mar 2018

One- and two-dimensional modes in the complex Ginzburg-Landau equation with a trapping potential

Thawatchai Mayteevarunyoo[1], Boris A. Malomed[2,3], and Dmitry V. Skryabin[3,4]

[1]*Department of Electrical and Computer Engineering, Faculty of Engineering, Naresuan University, Phitsanulok 65000, Thailand*

[2]*Department of Physical Electronics, School of Electrical Engineering, Faculty of Engineering, and Center for Light-Matter Interaction, Tel Aviv University, Tel Aviv 69978, Israel*

[3]*ITMO University, St. Petersburg 197101, Russia*

[4]*Department of Physics, University of Bath, Bath, BA2 7AY, UK*

Abstract

We propose a new mechanism for stabilization of confined modes in lasers and semiconductor microcavities holding exciton-polariton condensates, with spatially uniform linear gain, cubic loss, and cubic self-focusing or defocusing nonlinearity. We demonstrated that the commonly known background instability driven by the linear gain can be suppressed by a combination of a harmonic-oscillator trapping potential and effective diffusion. Systematic numerical analysis of one- and two-dimensional (1D and 2D) versions of the model reveals a variety of stable modes, including stationary ones, breathers, and quasi-regular patterns filling the trapping area in the 1D case. In 2D, the analysis produces stationary modes, breathers, axisymmetric and rotating crescent-shaped vortices, stably rotating complexes built of up to 8 individual vortices, and, in addition, patterns featuring vortex turbulence. Existence boundaries for both 1D and 2D stationary modes are found in an exact analytical form, and an analytical approximation is developed for the full stationary states.

I. INTRODUCTION

Formation of optical patterns in nonlinear media, that include pump, gain and loss mechanisms, such as laser cavities, as well as in many other physical settings, is frequently modeled by complex Ginzburg-Landau equations (CGLEs) [1]-[4]. In many cases, modes of primary interest are localized ones, supported by a stable balance between the gain and loss, as well as between the self-focusing nonlinearity and transverse diffraction, thus forming dissipative solitons [5]-[7]. In particular, the simplest one-dimensional (1D) cubic CGLE gives rise to exact localized solutions in the form of sech solitons with the phase chirp [8, 9]. However, a well-known problem for this simplest solution is that it is unstable, because the spatially uniform linear gain renders the zero background of the solitons unstable. One possibility for stabilization of dissipative solitons is offered by the adoption of the cubic-quintic nonlinearity, in which case the linear gain is replaced by linear loss, making the background stable, while the gain is supplied by the cubic term, and the quintic dissipation provides for the overall stabilization of the model [10]. In optics, this model can be realized using a combination of a usual linear amplifier with a saturable absorber [11, 12]. In particular, the CGLE with the cubic-quintic nonlinearity readily creates stable fundamental 2D dissipative solitons and their generalizations with the intrinsic vorticity [13]. These solitons can be additionally stabilized by the addition of the harmonic-oscillator (HO) trapping potential to the model, which also helps to build stable rotating two- and three-vortex complexes trapped in this potential [14].

On the other hand, keeping the nonlinearity in the basic cubic form, stable 1D dissipative solitons were predicted in two-component systems, where the additional lossy component, linearly-coupled to the gain-carrying one, provides for the stabilization of the background [15]-[16]. In particular, assuming that the nonlinearity is present only in the active component, it is possible to find 1D dissipative solitons analytically, in the form of the chirped sech ansatz, which have a considerable stability domain [19]. In single-component settings with the cubic-only nonlinearity, stability of localized modes can also be secured if the linear gain is supplied in a confined area embedded inside a linear-loss background [20, 21].

Another approach to the stabilization of 1D dissipative solitons in the cubic medium was elaborated in Ref. [22], also using spatial inhomogeneity, but in a different form: the instability of the background induced by the linear spatially uniform gain can be suppressed

if the local coefficient of the cubic losses grows from the center to periphery faster than $|x|$. While this setting seems somewhat "exotic", it is interesting to test a possibility to build a more straightforward one, by combining the uniform linear gain and the HO trapping potential, $\sim x^2$, which may approximate deep guiding channels in various photonic settings [23, 24]. Indeed, although the linear gain amplifies perturbations far from the localized mode, the HO potential will push the perturbations towards the core area, where the localized mode may have a chance to suppress them with the help of the usual cubic loss. Recently, this possibility was tested in the two-dimensional (2D) model of a spinor (two-component) exciton-polariton condensate, with its components linearly mixed by the spin-orbit coupling (SOC) [25]. It was found that the interplay of the linear gain, HO trap, complex cubic nonlinearity, and SOC gives rise to families of stable 2D dissipative solitons in the form of mixed modes (so called because they combine zero-vorticity and vortex terms in each component), vortex-antivortex complexes, and semi-vortices (which feature vorticity in one component, provided that the Zeeman splitting between the components is present). However, the stability is only possible if the model also includes an imaginary part (η) of the diffraction coefficient, i.e., spatial filtering [26]. It may represent ionization of the medium [27], or relatively poor finesse of the laser cavity [28]-[30], or diffusion of excitons in semiconductor microcavities [31]-[35]). The stability of the above-mentioned 2D confined modes is secured if η exceeds a certain threshold value.

These results suggest a possibility to consider a setting in a still more fundamental form of the single-component cubic CGLE with the linear gain, spatial filtering (effective diffusion), and the HO potential, in 1D and 2D geometries alike. The model may apply both to the optical laser cavities and microcavities populated by the exciton-polariton condensate. This analysis is the objective of the present work and it will be chiefly performed by means of numerical methods. Nevertheless, the existence boundary for dissipative solitons is obtained in an *exact analytical form*, in the 1D and 2D cases alike, due to the fact that the linearized form of both the 1D and 2D CGLE, including the spatial filtering and HO potential, admits (novel) exact solutions.

The paper is organized as follows. The models, both 1D and 2D ones, are introduced in Section II, where we also produce exact analytical solutions of the linearized CGLEs, which determine the existence boundaries of the 1D and 2D confined states, and some additional approximate analytical results for nonlinear stationary modes. Numerical results for the 1D

and 2D models are reported, severally, in Sections III and IV. It is found that the parameter space of the 1D CGLE is populated by stable stationary modes or breathers (the latter occupying a narrow stripe) and persistent multi-peak quasi-regular states, which fill out the entire spatial domain confined by the HO potential. The 2D model also gives rise to stable stationary modes and breathers, as well as to vortices (both isotropic ones and deformed rotating "crescents") and rotating robust multi-vortex bound states, with the net vorticity up to $S = 8$. The parameter space of the 2D model also features an area of vortex turbulence. The paper is concluded by Section V.

II. THE MODEL AND ANALYTICAL RESULTS

A. Complex Ginzburg-Landau equations

All the ingredients of the setting under the consideration, which was outlined in the introduction, are included in the 1D CGLE, with spatial coordinate x, which governs the evolution of local amplitude ψ of the electromagnetic wave:

$$i\frac{\partial \psi}{\partial t} = -\frac{1}{2}(1 - i\eta)\frac{\partial^2 \psi}{\partial x^2} \\ -\sigma|\psi|^2\psi + i(\gamma - \Gamma|\psi|^2)\psi + \frac{1}{2}\Omega^2 x^2 \psi. \tag{1}$$

Here $\eta \geq 0$ is the above-mentioned effective diffusivity (in particular, for excitons in a semiconductor microcavity), $\gamma > 0$ and $\Gamma > 0$ are, respectively, the linear gain and cubic loss, the nonlinearity coefficient takes one of three normalized values,

$$\sigma = +1, 0, -1, \tag{2}$$

with $+1$ and -1 corresponding, severally, to the self-focusing and defocusing, and coefficient Ω^2 determines the strength of the trapping HO potential. Variable t in Eq. (1) is the temporal one in the model of the exciton-polariton condensate, or propagation coordinate in the model of the planar laser cavity in optics. On the other hand, a confined 1D laser cavity may be described by Eq. (1) with t remaining the temporal variable, similar to models of the Lugiato-Lefever type [36]. It is relevant to mention that more fundamental models of laser cavities are based on coupled equations of the Maxwell-Bloch type; however, in many case, the atomic degrees of freedom may be adiabatically eliminated, reducing the model to the field-evolution equation of the CGLE type [37].

It is also relevant to mention that, depending on a particular setting, the instability of the zero state in laser cavities may emerge at a finite wavenumber, rather than at the infinitely small one (the short-wave instability, instead of its long-wave counterpart). In that case, the basic nonlinear model is represented not by the CGLE, but by the complex Swift-Hohenberg equation [38]. The latter model may be a subject for a separate work.

Keeping normalization condition (2), one can still perform rescaling of Eq. (1), so as to make coefficients γ and Γ equal, therefore we also fix relation

$$\gamma = \Gamma. \tag{3}$$

Thus, Eq. (1), subject to conditions (2) and (3), has three free coefficients: η, $\gamma = \Gamma$, and Ω^2. The sign coefficient (2) should be added to this set of control parameters.

Stationary states in the polariton condensate with real chemical potential μ (alias propagation constant, $-\mu$, in the models of planar laser cavities, with t playing the role of the propagation coordinate) are looked for as solutions to Eq. (1) in the form of

$$\psi\left(x,t\right) = e^{-i\mu t}u(x), \tag{4}$$

with complex function $u(x)$ satisfying the equation

$$\begin{aligned} \mu u = -\frac{1}{2}(1-i\eta)\frac{d^2u}{dx^2} \\ -\sigma|u|^2u + i(\gamma - \Gamma|u|^2)u + \frac{1}{2}\Omega^2x^2u. \end{aligned} \tag{5}$$

Stationary states are characterized by the integral power (alias the norm),

$$N = \int_{-\infty}^{+\infty} |u(x)|^2\, dx, \tag{6}$$

even if its not a dynamical invariant of the present dissipative model.

The stability analysis for stationary states (4) is based on introducing a perturbed solution,

$$\psi(x,t) = e^{-i\mu t}\left\{u(x) + \varepsilon\left[v(x)\exp\left(\lambda t\right) + w^*(x)\exp\left(\lambda^* t\right)\right]\right\}, \tag{7}$$

where ε determines the smallness of the perturbation, $v(x)$ and $w(x)$ are complex components of the perturbation eigenmode, and complex λ is the respective stability eigenvalue. The substitution of ansatz (7) in Eq. (1) and linearization with respect to ε leads to the system

of stationary linear equations:

$$\begin{aligned}
(\mu + i\lambda - i\gamma)\, v = -\frac{1}{2}(1 - i\eta)\frac{d^2 v}{dx^2} + \frac{1}{2}\Omega^2 x^2 v \\
-2\,(\sigma + i\Gamma)\,|u(x)|^2 v - (\sigma + i\Gamma)\,(u(x))^2\, w, \\
(\mu - i\lambda + i\gamma)\, w = -\frac{1}{2}(1 + i\eta)\frac{d^2 w}{dx^2} + \frac{1}{2}\Omega^2 x^2 w \\
-2\,(\sigma - i\Gamma)\,|u(x)|^2 w - (\sigma - i\Gamma)\,(u^*(x))^2\, v.
\end{aligned} \tag{8}$$

Instability is accounted for by eigenvalues with $\mathrm{Re}(\lambda) > 0$.

The 2D model is based on the corresponding version of Eq. (1), which is written, in terms of the polar coordinates, (r, θ), as

$$\begin{aligned}
i\frac{\partial \psi}{\partial t} = -\frac{1}{2}(1 - i\eta)\left(\frac{\partial^2}{\partial r^2} + \frac{1}{r}\frac{\partial}{\partial r} + \frac{1}{r^2}\frac{\partial^2}{\partial \theta^2}\right)\psi \\
-\sigma|\psi|^2\psi + i(\gamma - \Gamma|\psi|^2)\psi + \frac{1}{2}\Omega r^2 \psi,
\end{aligned} \tag{9}$$

with coefficients subject to conditions (2) and (3). Its stationary solutions with integer vorticity $S = 0, 1, 2, ...$ are looked for as

$$\psi\,(x, y, t) = e^{-i\mu t + iS\theta} u(r), \tag{10}$$

where complex function $u(r)$ satisfies the radial equation:

$$\begin{aligned}
\mu u = -\frac{1}{2}(1 - i\eta)\left(\frac{d^2}{dr^2} + \frac{1}{r}\frac{d}{dr} - \frac{S^2}{r^2}\right)u \\
-\sigma|u|^2 u + i(\gamma - \Gamma|u|^2)u + \frac{1}{2}\Omega r^2 u,
\end{aligned} \tag{11}$$

with boundary condition $u(r) \sim r^S$ at $r \to 0$. The integral power (norm) of the 2D state is

$$N = 2\pi \int_0^\infty |u(r)|^2\, r dr. \tag{12}$$

For the stability test, perturbed 2D solutions were looked for as [cf. Eq. (7)]

$$\begin{aligned}
\psi(x, t) = \left\{e^{-i\mu t} u(r) + \varepsilon\,[v(xr)\exp(\lambda t + im\theta)\right. \\
\left. + w^*(r)\exp(\lambda^* t - im\theta)]\right\},
\end{aligned} \tag{13}$$

where integer m is an independent angular index of the perturbation mode, and the radial

equations for perturbation amplitudes are

$$(\mu + i\lambda - i\gamma)\, v = -\frac{1}{2}(1 - i\eta)\left[\frac{d^2}{dr^2} + \frac{1}{r}\frac{d}{dr} - \frac{(S+m)^2}{r^2}\right] v$$
$$+\frac{1}{2}\Omega^2 r^2 v - 2\,(\sigma + i\Gamma)\,|u(x)|^2 v - (\sigma + i\Gamma)\,(u(x))^2\, w,$$
$$(\mu - i\lambda + i\gamma)\, w = -\frac{1}{2}(1 + i\eta)\left[\frac{d^2}{dr^2} + \frac{1}{r}\frac{d}{dr} - \frac{(S-m)^2}{r^2}\right] w$$
$$+\frac{1}{2}\Omega^2 r^2 w - 2\,(\sigma - i\Gamma)\,|u(x)|^2 w - (\sigma - i\Gamma)\,(u^*(x))^2\, v. \tag{14}$$

This eigenvalue problems defined by Eqs. (8) and (14) were solved by means of numerical methods.

B. Analytical solutions

The amplitude of stationary states vanishes at their existence boundary, where, accordingly, one-dimensional equation (5) is replaced by its linearized version,

$$\mu u = -\frac{1}{2}(1 - i\eta)\frac{d^2 u}{dx^2} + i\gamma u + \frac{1}{2}\Omega^2 x^2 u. \tag{15}$$

Straightforward consideration of Eq. (15) demonstrates that it gives rise to an *exact* ground-state (GS) solution, with arbitrary amplitude A_0,

$$u_{\rm lin}^{\rm (1D)}(x) = A_0 \exp\left(-\frac{\Omega}{2\sqrt{1 - i\eta}}x^2\right), \tag{16}$$

$$\mu_{\rm lin}^{\rm (1D)} = \frac{\Omega\eta}{2\sqrt{2\left(\sqrt{1+\eta^2} - 1\right)}}. \tag{17}$$

provided that diffusivity η is related to linear gain γ as follows:

$$\gamma_{\rm thr}^{\rm (1D)} = \frac{\Omega}{2\sqrt{2}}\sqrt{\sqrt{1+\eta^2} - 1}. \tag{18}$$

This exact solution follows the commonly known pattern of the GS wave function of the one-dimensional HO potential in quantum mechanics. However, the complex coefficient in front of the second derivative in Eq. (15) introduces an essential difference, in the form of the *spatial chirp* of the wave function (a phase term $\sim x^2$).

Equation (18) determines the existence threshold of the GSs of the full 1D nonlinear model, which are indeed found, in the numerical form, precisely at $\gamma > \gamma_{\rm thr}^{\rm (1D)}$, as shown

below. In the absence of the nonlinearity ($\sigma = \Gamma = 0$), Eq. (1) gives rise to an exponentially growing solution at $\gamma > \gamma_{\rm thr}^{\rm (1D)}$:

$$\psi_{\rm lin}^{\rm (1D)}(x) = A_0 \exp\left[\left(\gamma - \gamma_{\rm thr}^{\rm (1D)}\right) t\right] \times \exp\left(-\frac{\Omega}{2\sqrt{1-i\eta}} x^2\right). \tag{19}$$

Similarly, the linearized version of the 2D stationary equation (11),

$$\mu u = -\frac{1}{2}(1-i\eta)\left(\frac{d^2}{dr^2} + \frac{1}{r}\frac{d}{dr} - \frac{S^2}{r^2}\right) u + i\gamma u + \frac{1}{2}\Omega r^2 u, \tag{20}$$

gives rise to exact solutions for both the GS ($S = 0$) and vortices ($S \geq 1$):

$$u_{\rm lin}^{\rm (2D)}(r) = A_0 r^S \exp\left(-\frac{\Omega}{2\sqrt{1-i\eta}} r^2\right), \tag{21}$$

$$\mu_{\rm lin}^{\rm (2D)} = \frac{(1+S)\Omega\eta}{\sqrt{2\left(\sqrt{1+\eta^2}-1\right)}}, \tag{22}$$

the corresponding threshold being

$$\gamma_{\rm thr}^{\rm (2D)} = (1+S)\,\Omega\sqrt{\frac{1}{2}\left(\sqrt{1+\eta^2}-1\right)}. \tag{23}$$

These exact solutions follow the pattern of the GS and eigenstates carrying the orbital angular momentum for the two-dimensional HO potential, the difference from the quantum-mechanical wave functions being the presence of the *radial chirp*, i.e., a phase term $\sim r^2$.

At $\gamma > \gamma_{\rm thr}^{\rm (2D)}$, the parameter space of the 2D nonlinear model is populated by several types of robust static and dynamical modes, as shown below, while, in the absence of the nonlinearity ($\sigma = \Gamma = 0$), an exponentially growing solution to Eq. (9) is [cf. Eq. (19)]

$$\psi_{\rm lin}^{\rm (2D)}(r) = A_0 \exp\left[\left(\gamma - \gamma_{\rm thr}^{\rm (2D)}\right) t\right] \times r^S \exp\left(-\frac{\Omega}{2\sqrt{1-i\eta}} r^2\right).$$

For the 1D nonlinear model (1), an approximate analytical solution can be found in the case of $\sigma = 0$, $\Gamma > 0$ (i.e., if the nonlinearity is represented solely by the cubic loss), treating the gain and loss terms as small perturbations. In the zero-order approximation, the stationary solution is represented by the GS of the HO potential,

$u_0(x) = A_0^{(1\mathrm{D})} \exp\left(-\Omega x^2/2\right)$, $\mu = \Omega/2$ [cf. Eq. (16)], where amplitude A_0 is determined, in the first-order approximation, by the power-balance condition:

$$\int_{-\infty}^{+\infty} \left(\gamma |u|^2 - \Gamma |u|^4 - \frac{1}{2}\eta \left| \frac{du}{dx} \right|^2 \right) dx = 0. \tag{24}$$

The substitution of the zero-order wave function in Eq. (24) predicts the squared amplitude,

$$\left(A_0^{(1\mathrm{D})} \right)^2 = \frac{4\gamma - \Omega\eta}{2\sqrt{2}\Gamma}. \tag{25}$$

The norm (6) of the solution with amplitude (25) is

$$N = \frac{\sqrt{\pi}\left(4\gamma - \Omega\eta\right)}{2\sqrt{2\Omega}\Gamma}. \tag{26}$$

In particular, Eq. (26) predicts that nonzero states exist at $\gamma > \gamma_{\mathrm{thr}} = \Omega\eta/4$. For small η, this result agrees with the exact threshold given by Eq. (18).

A similar prediction can be elaborated for 2D vortex modes produced by Eq. (11) with $\sigma = 0$ and $\Gamma > 0$. In this case, the zero-order wave function is $u_0^{(2\mathrm{D})}(r) = A_0^{(2\mathrm{D})} r^S \exp\left(-\Omega r^2/2\right)$, cf. Eq. (21), while the 2D power-balance condition is

$$\int_0^{\infty} \left[\gamma |u|^2 - \Gamma |u|^4 - \frac{1}{2}\eta \left(\left| \frac{du}{dr} \right|^2 + \frac{S^2}{r^2}|u| \right) \right] r dr = 0. \tag{27}$$

The substitution of $u_0^{(2\mathrm{D})}(r)$ in Eq. (27) yields the result:

$$\left(A_0^{(2\mathrm{D})} \right)^2 = 2^{1+2S} \frac{S!}{(2S)!} \frac{\Omega^S}{\Gamma} \left(\gamma - \frac{1+S}{2}\Omega\eta \right), \tag{28}$$

which corresponds to the 2D integral power (12)

$$N = 2^{1+2S} \frac{\pi S!}{(2S)!} \left(\Omega\Gamma\right)^{-1} \left(\gamma - \frac{1+S}{2}\Omega\eta \right), \tag{29}$$

cf. Eq. (26). The threshold condition, following from Eq. (29), $\gamma > \gamma_{\mathrm{thr}}\left(1+S\right)/2$, in the limit of small η is consistent with the exact 2D threshold condition (23).

The analytical results, both exact and analytical ones, are compared to their numerical counterparts below.

III. BASIC RESULTS: THE 1D SETTING

Numerical solutions of stationary equations (5) and (11) were constructed by means of the squared-operator iterative method [39]. The evolution governed by Eqs. (1) and (9) was

simulated using the fourth-order split-step Fourier-transform algorithm. The integration domain with dimensions $-8 < x, y < +8$ was sufficient to accommodate all confined modes investigated herein. In most cases, the numerical grid of size 128×128 was sufficient to produce the modes with necessary accuracy. The stability and instability of all stationary modes, predicted by the numerical solution of linearized equations (8), was accurately corroborated by direct simulations. As said above, control parameters of the model are $\gamma = \Gamma$ [see Eq. (3)], η, and Ω^2, as well as the discrete nonlinearity coefficient, $\sigma = -1, 0, +1$ in Eq. (2).

First, in the absence of losses, $\gamma = \Gamma = \eta = 0$, it is easy to construct a family of real GS solutions of Eq. (5) for either sign of σ, which correspond to stable solutions of Eq. (1). For $\sigma = +1$ and -1 (the self-focusing/defocusing cubic term), the shape of the GS is close, respectively, to that of the usual bright soliton placed at the bottom of the HO potential trap, or to the GS predicted by the Thomas-Fermi (TF) approximation [40]. In both cases, the families of the GSs are characterized by dependences of their integral power (6) on chemical potential μ, as shown in Fig. 1. Naturally, in the limit of $N \to 0$ the branches originate from value $\mu = \Omega/2$, which corresponds to the GS of the HO potential, while in the limit of $N \to \infty$ the dependences are determined, respectively, by the free-space soliton solution and the TF approximation : $N_{\rm sol}(\mu) = 2\sqrt{-2\mu}$; $N_{\rm TF}(\mu) = 2(3\Omega)^{-1}\,(2\mu)^{3/2}$.

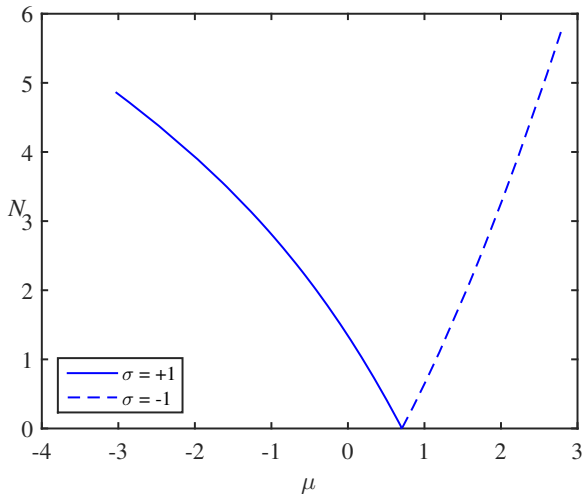


FIG. 1: The integral power (norm) of 1D ground states in the conservative limit, $\gamma = \Gamma = \eta = 0$, vs. the chemical potential, for the self-focusing ($\sigma = +1$) and defocusing ($\sigma = -1$) signs of the cubic term, with the strength of the HO potential $\Omega^2 = 2$.

Proceeding to the 1D model with $\gamma = \Gamma = 1$, we note, first, that all the stationary modes are unstable in the absence of the effective diffusion, $\eta = 0$, similar to what was reported in Ref. [25]. This instability transforms static modes into quasi-turbulent states which fill the entire space admitted by the HO trapping potential, as shown in Fig. 2.

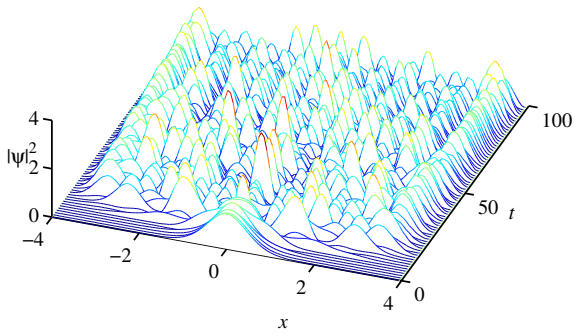


FIG. 2: The unstable evolution of a numerically constructed stationary trapped 1D mode for $\gamma = \Gamma = 1.0$, $\eta = 0$ (no diffusivity), $\Omega^2 = 2$, and $\sigma = +1$ (the self-focusing cubic term).

Robust stationary and dynamical states are found in the presence of $\eta > 0$: stable stationary GS modes existing at relatively large values of η [Fig. 3(a)]; persistent breathers, spontaneously emerging from some unstable stationary modes at smaller η [Fig. 3(b)]; and quasi-regular multi-peak periodically oscillating states, developing from unstable stationary modes at small η [Fig. 4]. In the limit of $\eta \to 0$, the latter pattern goes over into the quasi-turbulent one displayed in Fig. 2. The increase of η naturally leads to simplification of the quasi-regular patterns via the decrease of the number of peaks, from seven in Fig. 4(a) to five in 4(b), to three 4(c) and, eventually, to one in Fig. 4(d). The latter dynamical mode is close to a regular breather, cf. Fig. 3(b).

The results obtained in the case of self-focusing, $\sigma = +1$, are summarized in Fig. 5, where panel (a) shows the numerically found dependence of the integral power, N on the crucially important control parameter, η, and panel (b) presents the findings in the form of stability map displayed in the plane of $\gamma = \Gamma$ and η. In particular, we stress that a numerically found existence boundary for stable GSs, shown by the black dashed line in (b), *precisely* coincides with the analytical prediction given by Eq. (18), which is shown by the red dashed line. Further, we observe that vast areas populated by stable GSs and persistent quasi-regular states are separated by a narrow sliver supporting stable breathers. We also stress that no

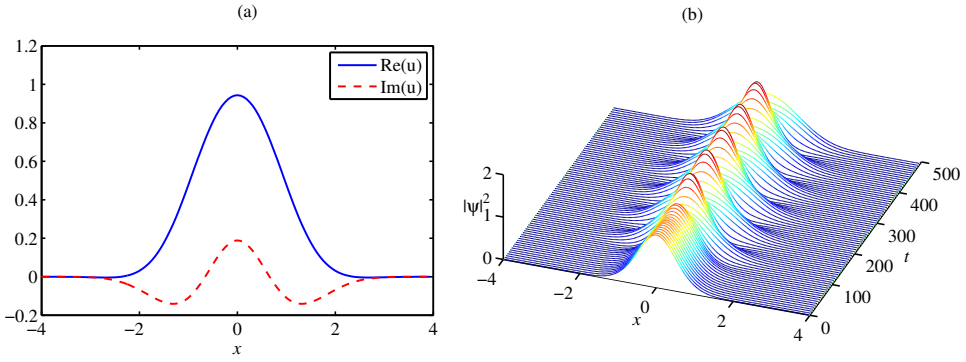


FIG. 3: Typical examples of robust dynamical regimes in the 1D model. (a) Real and imaginary parts of a typical stable stationary ground-state mode, found at $\eta = 0.8$, $\Omega^2 = 2$. The chemical potential and integral power (norm) of this mode are $\mu = 0.1714$ and $N = 1.4120$. (b) A persistent breather spontaneously generated by an unstable stationary mode, at $\eta = 0.3$. In both cases, $\gamma = \Gamma = 1$, $\Omega^2 = 2$, and $\sigma = +1$ (self-focusing).

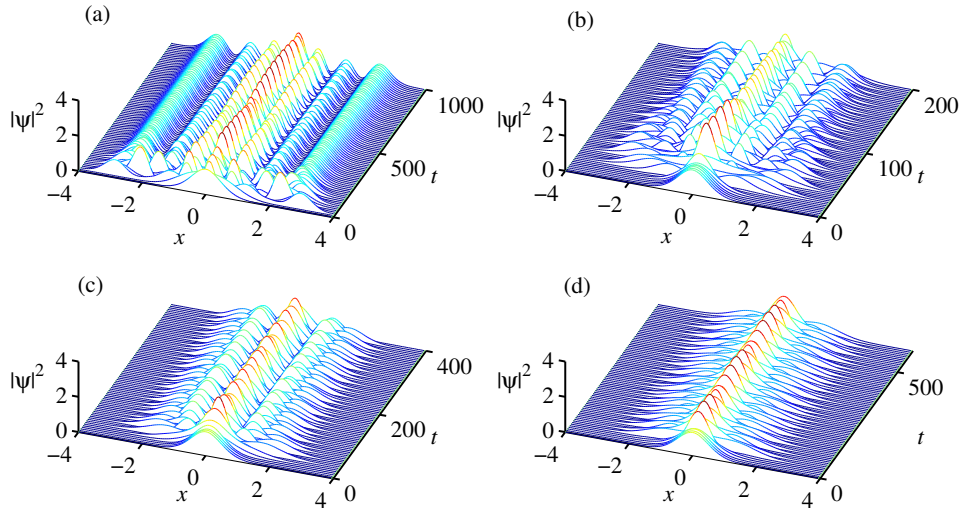


FIG. 4: Robust quasi-regular oscillatory states with seven (a), five (b), three (d), and single (d) peaks, developing from unstable stationary modes at $\eta = 0.05, 0.10, 0.15$, and 0.2, respectively. Other parameters are the same as in Fig. 3.

case of bistability was produced by the systematic numerical analysis.

In the 1D model with the self-focusing cubic term, $\sigma = +1$, the results obtained for other values of the HO potential strength, Ω^2, are quite similar to those displayed above for $\Omega^2 = 1$. Further, the results also remain similar for the defocusing sign of the cubic term, $\sigma = -1$, as well as in the 1D model with $\sigma = 0$, where the nonlinearity is represented solely

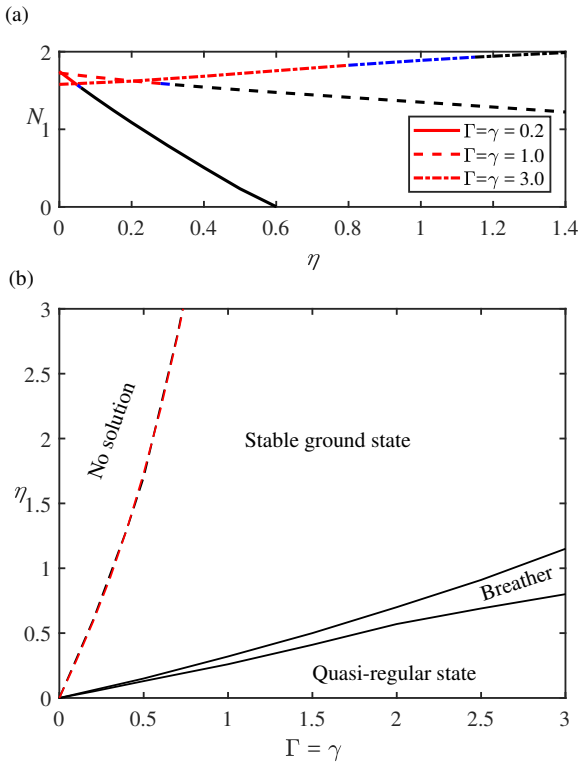


FIG. 5: (a) The integral power (norm) of the numerically generated stationary 1D modes vs. diffusivity η, for $\sigma = +1$ (the self-focusing cubic term), $\Omega^2 = 2$, and $\gamma = \Gamma = 0.2$, 1.0, and 3.0 (solid, dashed, and dotted lines, respectively). The stability is identified by colors: red corresponds to unstable stationary modes generating quasi-regular states; blue corresponds to unstable modes developing into breathers; and black represents stable stationary modes. (b) The stability map for different robust stationary and dynamical states, labeled in the plane of ($\gamma = \Gamma$,η), for $\Omega^2 = 2$ and $\sigma = +1$. The dashed line is the existence boundary for the stationary states, as predicted by Eq. (18). It completely coincides with the numerically found counterpart.

by the cubic loss, $\Gamma > 0$. These conclusions are illustrated by Fig. 6, which summarizes the results for $\sigma = 0$ and $\Omega^2 = 6$, in the same way as it is done in Fig. 5 for $\sigma = +1$ and $\Omega^2 = 2$. In particular, the magenta line in panel 5 demonstrates that the analytical approximation, elaborated for $\sigma = 0$ in the form of Eq. 26), is an accurate one. Overlapping black and red dashed curves display, severally, the numerically found and analytically predicted [see Eq. (18)] existence boundaries for the stationary GS modes.

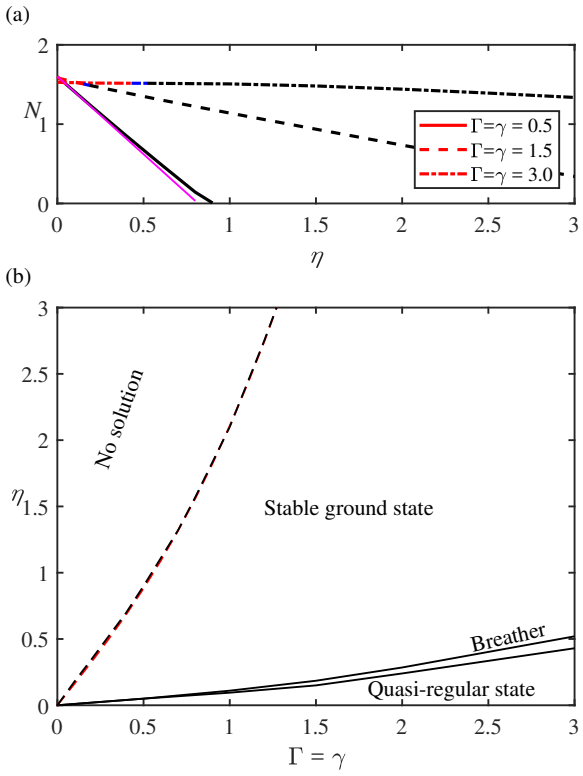


FIG. 6: The same as in Fig. 5, but for the 1D model with $\sigma = 0$ and $\Omega^2 = 6$. The magenta solid line in (a) additionally displays the analytical approximation (26) for $\gamma = \Gamma = 0.5$.

IV. BASIC RESULTS: THE 2D SETTING

In the 2D model, the systematic numerical analysis has identified several types of stationary and dynamical states. First, similar to the 1D case, the largest stability area is found for stationary GS states, which are trapped isotropic modes, see an example in Fig. 7. Next, persistent axisymmetric breathers, developing from unstable stationary states, are found too, although in a small parameter area (see below). An example of the breather is displayed in Fig. 8

The decrease of η leads, as in the 1D model, to destabilization of the stationary modes. The evolution of unstable modes generates a variety of different dynamical states featuring vortex structures, cf. Refs. [41, 42], where the 2D CGLE with the cubic-quintic nonlinearity and a radially localized linear gain (but without a trapping potential and diffusion) also gave rise to a large number of different vortical modes; stable complexes built of one, two, or three vortices were reported too in the study of the cubic-quintic CGLE model with the uniform linear loss and trapping HO potential [14]. Among such structures, we first identify stable

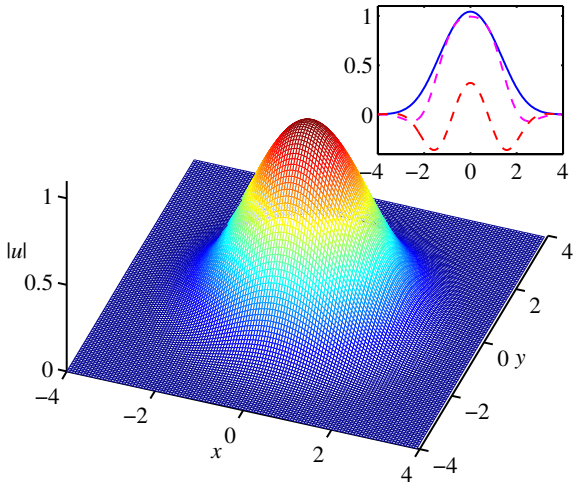


FIG. 7: A stable 2D GS, numerically found for $\sigma = 0$, $\Gamma = \gamma = 3.0$, $\eta = 1.5$, and $\Omega^2 = 2$. The inserted panel shows radial profiles, along $y = 0$, of the amplitude $|u(x)|$ (blue), as well as real (magenta) and imaginary (red) parts of $u(x)$.

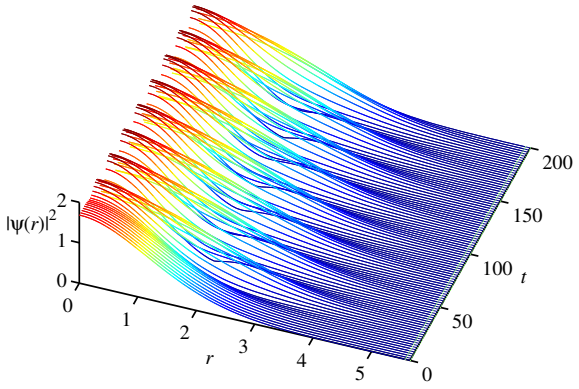


FIG. 8: A persistent isotropic breather generated by an unstable stationary mode at $\sigma = +1$, $\Gamma = \gamma = 2.3$, $\eta = 0.6$, and $\Omega^2 = 2$.

axisymmetric vortices with topological charge $S = 1$, see an example in 9. The spontaneous generation of vorticity in the dissipative medium is explained by the fact that, originally, it generates a vortex-antivortex pair, whose antivortex component disappears in the peripheral area. The axisymmetric vortices have also been produced as stationary solutions of Eq. (11), and their stability has been identified by means of Eq. (14).

Further decrease of η causes destabilization of the axisymmetric vortices and replaces them, depending on values of other parameters (especially, σ), either by rotating azimuthally

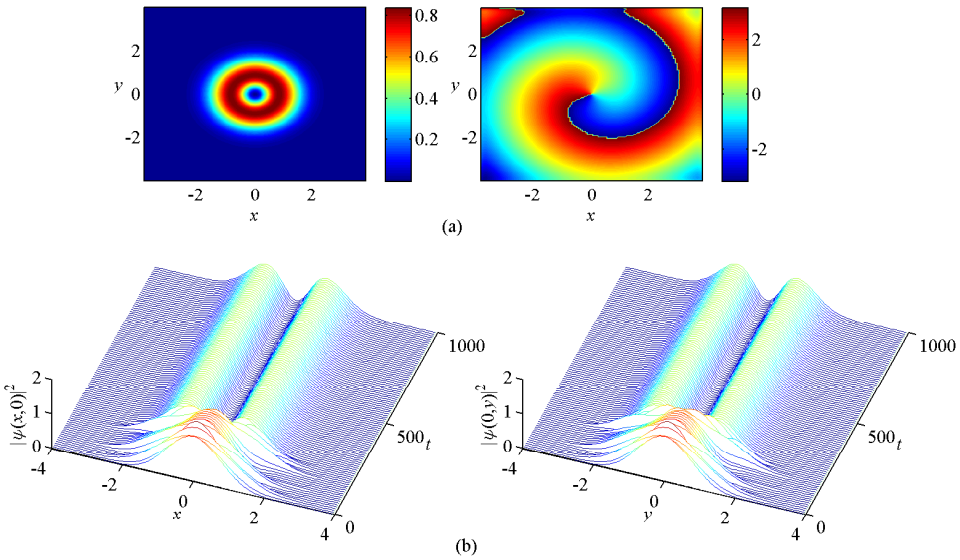


FIG. 9: (a) The local-intensity $[|u(x,y)|^2]$ and phase structure of a stable axisymmetric vortex spontaneously generated by an unstable stationary mode, at $\sigma = 0$, $\Gamma = \gamma = 2.5$, $\eta = 0.6$, and $\Omega^2 = 2$. (b) The evolution of the local intensity in the x and y cross-sections, illustrating the spontaneous transformation of the unstable stationary mode into the isotropic vortex.

nonuniform vortices with a crescent shape and $S = 1$, or by rotating two-vortex complexes, with $S = 2$ (see examples in Fig. 10), or by a state which may be categorized as vortex turbulence, see Fig. 11. In particular, the crescents emerge only in the case of the self-focusing cubic nonlinearity, $\sigma = +1$. Subsequent decrease of η reveals transition to more complex rotating sets of vortices, which feature the net topological charge up to $S = 8$, see a set of typical examples in Fig. 10 (in this particular figure, the largest topological charge of a stable multi-vortex complex is $S_{\max} = 7$; a peculiarity of the latter bound state, displayed in the bottom panels of Fig. 10, is that it has one vortex placed at the center, surrounded by a rotating necklace of six satellites). Eventually, at very small values of η, the 2D model gives rise to the above-mentioned vortex-turbulent state, an example of which is presented in Fig. 11.

Numerically measured characteristics of the rotating complexes displayed in Fig. 10, *viz.*, the values of their radius, defined as the distance of maxima of the local intensity from the rotation pivot, and the angular velocity of the rotation, are collected in Table I. Naturally, the radius tends to grow with the increase of the total number of individual vortices, S. The value of radius ρ of the ring-shaped crescent vortex (as well as the radius of the isotropic

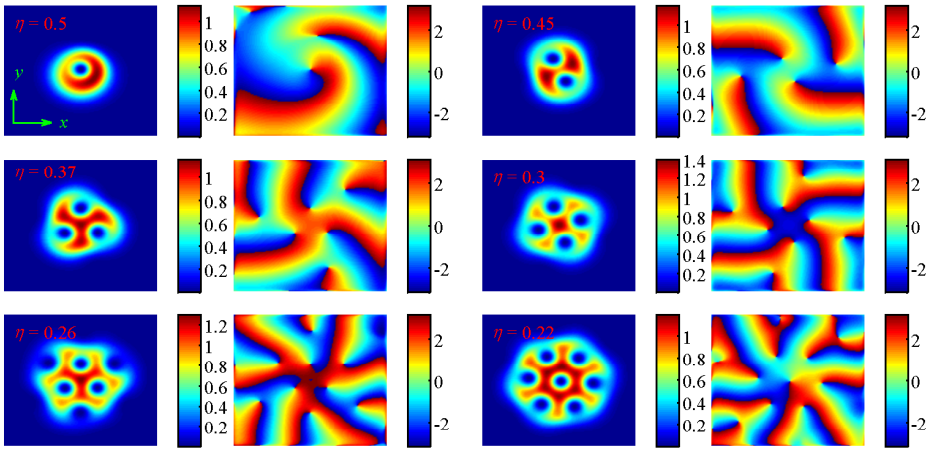


FIG. 10: A sequence of stably rotating states produced by the simulations of the 2D model for $\sigma = +1$, $\Gamma = \gamma = 2.5$, and $\Omega^2 = 2$, at decreasing values of diffusivity η (which are indicated in the panels): a crescent vortex ($S = 1$), and multi-vortex complexes with $S = 2, 3, 4, 6$, and 7. At $\eta > 0.5$, the model supports a a stable axisymmetric vortex with $S = 1$, while at $\eta < 0.22$ a transition to vortex turbulence occurs. In all panels, spatial scales are the same as in Fig. 9(a).

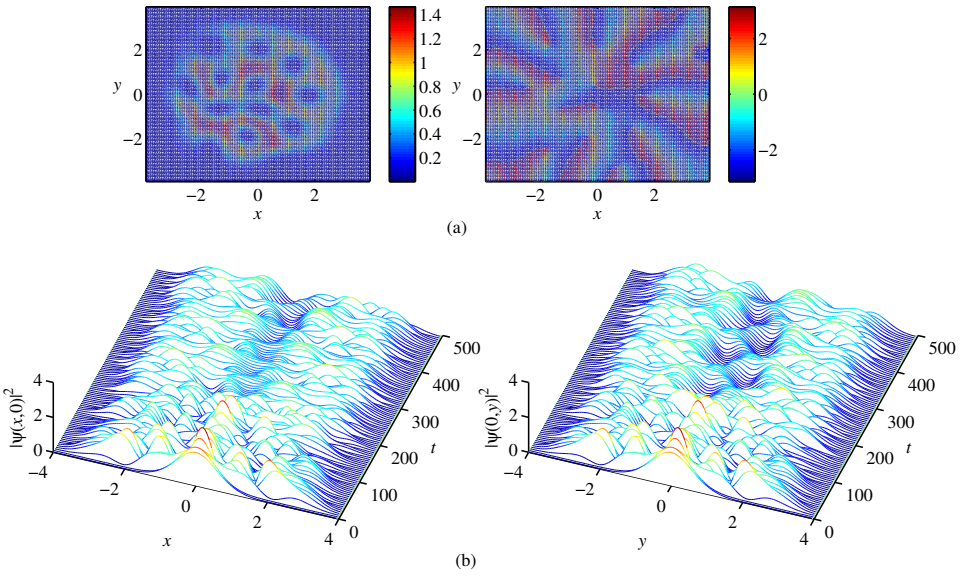


FIG. 11: An example of the vortex-turbulent state, found for $\sigma = 0$, $\gamma = \Gamma = 2$, $\eta = 0.1$, and $\Omega^2 = 2$. (a) Snapshots of the local-intensity, $|\psi(x, y)|^2$, and phase patterns (left and right panels, respectively), produced, at $t = 1000$, by simulations initiated with an unstable stationary state. (b) The respective evolution of the local intensity, shown in the x- and y- cross sections.

TABLE I: Characteristics of rotating complexes built of S individual vortices shown in Fig. 10, i.e., with $\sigma = +1$, $\Gamma = \gamma = 2.5$, and $\Omega^2 = 2$ ($S = 1$ corresponds to the rotating crescent-shaped vortex).

Total vorticity	the effective radius	ω
$S = 1$ ($\eta = 0.50$)	0.8359	3.927
$S = 2$ ($\eta = 0.45$)	0.7500	1.6526
$S = 3$ ($\eta = 0.37$)	1.0000	1.5932
$S = 4$ ($\eta = 0.30$)	1.1250	1.5150
$S = 6$ ($\eta = 0.26$)	1.4688	1.4956
$S = 7$ ($\eta = 0.22$)	1.7500	1.4952

vortex, when it is stable) can be easily explained as one at which the density of the eigenstate with $S = 1$ in the linear Schrödinger equation with the HO potential attains the maximum, which is $\rho_0 = \Omega^{-1/4}$. Indeed, $\rho_0(\Omega = 2) \approx 0.8409$ is almost identical to the numerically determined radius for $S = 1$ in Table I. As concerns the angular velocity, ω, of the rotating crescent, we note that, for a narrow ring of radius ρ, the linear Schrödinger equation produces an elementary result, $\omega = S/\rho^2$. In reality, the crescent, displayed in the top row of Fig. 10, is not quite narrow, and the comparison of this formula with the respective angular velocity given in Table I suggests that ω is determined by the inner layer of the crescent, which has $\rho \simeq 0.5$. It is relevant to note that the rotation velocity of the crescent-shaped vortex with $S = 1$ is essentially higher than in all the complexes with $S \geq 2$.

Note that the sequence of multi-vortex complexes, displayed in Fig. 10 for $\sigma = +1$ (the self-focusing sign of the nonlinearity), does not include a bound state of five vortices. Actually, such a stable state can be found too, but for $\sigma = -1$, as shown in Fig. 12.

Results produced by systematic numerical analysis of the 2D model are summarized in Figs. 13 and 14 for $\sigma = 0$ and $\sigma = +1$, respectively, fixing $\Omega^2 = 2$. For other values of Ω^2, the plots are quite similar to the ones displayed here. Furthermore, for $\sigma = -1$, the plots are also similar to what is shown in Fig. 13(b) for $\sigma = 0$. We stress that the analytical existence boundary for the stationary mode, predicted by Eq. (23), is completely identical to its numerically found counterpart. Comparing these stability maps with their counterparts reported above for the 1D model, cf. Figs. 6 for $\sigma = 0$ and 5 for $\sigma = +1$, we conclude

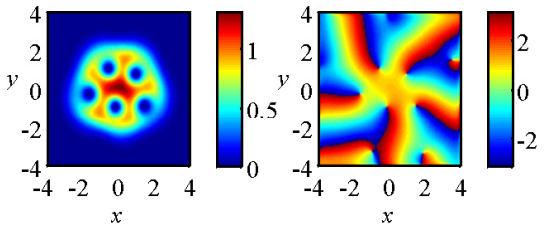


FIG. 12: The local-intensity and phase structure of a stably rotating 5-vortex bound state found for $\sigma = -1$, $\Gamma = \gamma = 2.0$, $\eta = 0.23$, and $\Omega^2 = 2$.

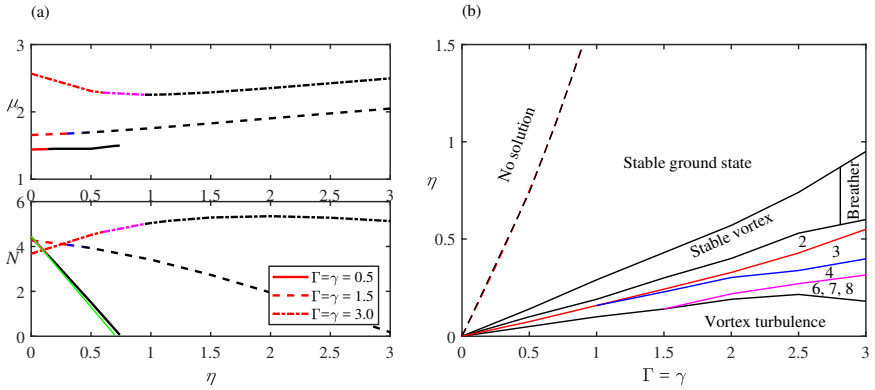


FIG. 13: (a) The integral power (norm) of numerically found 2D stationary modes, given by Eq. (12), vs. diffusivity η for $\sigma = 0$, $\Omega^2 = 2$, and $\gamma = \Gamma = 0.5$, 1.5, and 3.0 (solid, dashed, and dotted lines, respectively). The stability is identified by colors: red, blue, and magenta imply, severally, the transformation into vortex tubulence, stable axisymmetric vortices, and breathers, while black curves represent families of stable stationary modes. The green solid line displays the analytical approximation (29) for $\gamma = \Gamma = 0.5$. (b) Stability borders in the plane of $(\gamma = \Gamma, \eta)$ for $\sigma = 0$ and $\Omega^2 = 1$. The analytical existence boundary, $\eta_{\rm thr}^{(2D)}$, predicted by Eq. (23), and its numerically identified counterpart are shown, respectively, by red and black dashed lines, which completely overlap. Digits in subregions represent the number of individual vortices in rotating complexes populating these subregions. In particular, 1 implies the presence of the single ($S = 1$) rotating crescent-shaped vortex, different from the axisymmetric vortex in the area of "Stable vortex".

that the axisymmetric vortices with $S = 1$ and the vortex-turbulent states play, roughly speaking, the same role as, respectively, breathers and quasi-regular patterns in 1D, while the multi-vortex bound states do not have their 1D counterparts.

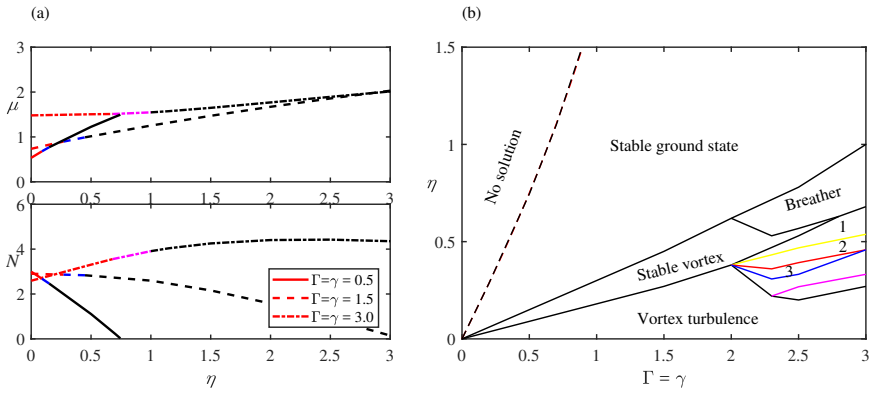


FIG. 14: The same as in Fig. 13, but for $\sigma = +1$.

V. CONCLUSION

We have demonstrated a new mechanism for the stabilization of confined modes in the 1D and 2D CGLEs (complex Ginzburg-Landau equations) with the cubic-only nonlinearity and the spatially uniform linear gain. Namely, we have found that the background instability is suppressed by the combination of the HO (harmonic-oscillator) trapping potential and effective diffusion. Analytical solutions for the linearized version of the CGLE provide existence boundaries for trapped modes, which are exactly confirmed by numerical results. Our numerical analysis has produced a set of stable stationary modes, persistent breathers, and more complex patterns, *viz.*, quasi-regular multi-peak structures in 1D, and vortices (axisymmetric and rotating deformed crescent-shaped ones), and rotating multi-vortex complexes, with the net topological charge up to $S = 8$, in 2D. The models addressed in this work apply to laser cavities and semiconductor microcavities with exciton-polariton condensates.

Funding

Thailand Research Fund (grant BRG6080017); The Royal Society (grant IE 160465); Israel Science Foundation (grant 1286/17); ITMO University Visiting Professorship (Government of Russia Grant 074-U01); H2020 (691011, Soliring).

[1] W. van Saarloos and P. C. Hohenberg, Fronts, pulses, sources and sinks in generalized complex Ginzburg-Landau equation, Physica D **56**, 303-367 (1992).

[2] H. Sakaguchi, Phase dynamics and localized solutions to the Ginzburg-Landau type amplitude equations, Prog. Theor. Phys. **89**, 1123-1146 (1993).

[3] I. S. Aranson and L. Kramer, The world of the complex Ginzburg-Landau equation, Rev. Mod. Phys. **74**, 99 (2002).

[4] N. N. Rosanov, *Spatial Hysteresis and Optical Patterns* (Springer, 2002).

[5] N. Akhmediev and A. Ankiewicz, eds., *Dissipative Solitons*, Vol. 661 of Lecture Notes in Physics (Springer, 2005).

[6] T. Ackemann, W. J. Firth, and G.-L. Oppo, Fundamentals and applications of spatial dissipative solitons in photonic devices, Adv. At. Mol. Opt. Phys. 57, 323-421 (2009).

[7] N. N. Rosanov, *Dissipative Optical Solitons: from Micro to Nano and Atto* (Fizmatlit, 2011) (in Russian).

[8] L. M. Hocking and K. Stewartson, Nonlinear response of a marginally unstable plane parallel flow to a 2-dimensional disturbance, Proc. R. Soc. A **326**, 289-313 (1972).

[9] N. R. Pereira and L. Stenflo, Nonlinear Schrödinger equation including growth and damping, Phys. Fluids **20**, 1733-1734 (1977).

[10] V. I. Petviashvili and A. M. Sergeev, Spiral solitons in active media with excitation thresholds, Dokl. AN SSSR (Sov. Phys. Dokl.) **276**, 1380-1384 (1984).

[11] A. Komarov, H. Leblond, and F. Sanchez, Quintic complex Ginzburg-Landau model for ring fiber lasers, Phys. Rev. E **72**, 025604(R) (2005).

[12] W. Renninger, A. Chong, and E. Wise, Dissipative solitons in normal-dispersion fiber lasers, Phys. Rev. A **77**, 023814 (2008).

[13] L.-C. Crasovan, B. A. Malomed, and D. Mihalache, Stable vortex solitons in the two-dimensional Ginzburg-Landau equation, Phys. Rev. E **63**, 016605 (2001).

[14] D. Mihalache, D. Mazilu, V. Skarka, B. A. Malomed, H. Leblond, N. B. Aleksić, and F. Lederer, Stable topological modes in two-dimensional Ginzburg-Landau models with trapping potentials, Phys. Rev. A **82**, 023813 (2010).

[15] B. A. Malomed and H. G. Winful, Stable solitons in two-component active systems, Phys. Rev. E **53**, 5365-5368 (1996).

[16] W. J. Firth and P. V. Paulau, Soliton lasers stabilized by coupling to a resonant linear system, Eur. Phys. J. D **59**, 13-21 (2010).

[17] P. V. Paulau, D. Gomila, P. Colet, N. A. Loiko, N. N. Rosanov, T. Ackemann, and W. J.

Firth, Vortex solitons in lasers with feedback, Opt. Express **18**, 8859-8866 (2010).

[18] A. Marini, D. V. Skryabin, and B. A. Malomed, Stable spatial plasmon solitons in a dielectric-metal-dielectric geometry with gain and loss, Opt. Express **19**, 6616-6622 (2011).

[19] J. Atai and B. A. Malomed, Exact stable pulses in asymmetric linearly coupled Ginzburg-Landau equations, Phys. Lett. A **246**, 412-422 (1998).

[20] Y. V. Kartashov, V. V. Konotop, V. A. Vysloukh, and D. A. Zezyulin, Guided modes and symmetry breaking supported by localized gain, in *Spontaneous Symmetry Breaking, Self-Trapping, and Josephson Oscillations*, ed. by B. A. Malomed (Springer-Verlag: Berlin and Heidelberg, 2013), pp. 167-200.

[21] B. A. Malomed, Spatial solitons supported by localized gain [Invited], J. Opt. Soc. Am. B **31**, 2460-2475 (2014).

[22] O. V. Borovkova, Y. V. Kartashov, V. A. Vysloukh, V. E. Lobanov, B. A. Malomed, and L. Torner, Solitons supported by spatially inhomogeneous nonlinear losses, Opt. Exp. **20**, 2657-2667 (2012).

[23] S. Raghavan and G. P. Agrawal, Spatiotemporal solitons in inhomogeneous nonlinear media, Opt. Commun. **180**, 377-382 (2000).

[24] D. A. Zezyulin, G. L. Alfimov, and V. V. Konotop, Nonlinear modes in a complex parabolic potential, Phys. Rev. A **81**, 013606 (2010).

[25] H. Sakaguchi, B. A. Malomed, and D. V. Skryabin, Spin-orbit coupling and nonlinear modes of the polariton condensate in a harmonic trap, New J. Phys. **19**, 08503 (2017).

[26] N. A. Veretenov, N. N. Rosanov, and S. V. Fedorov, Motion of complexes of 3D-laser solitons, Opt. Quant. Elect. **40**, 253-262 (2008).

[27] S. Skupin, L. Bergé, U. Peschel, F. Lederer, G. Méjean, J. Yu, J. Kasparian, E. Salmon, J. P. Wolf, M. Rodriguez, L. Wöste, R. Bourayou, and R. Sauerbrey, Filamentation of femtosecond light pulses in the air: Turbulent cells versus long-range clusters, Phys. Rev. E **70**, 046602 (2004).

[28] P. Coullet, L. Gil, and F. Rocca, Optical vortices, Opt. Commun. **73**, 403-408 (1989).

[29] J. Lega, J. V. Moloney, and A. C. Newell, Swift-Hohenberg equation for lasers, Phys. Rev. Lett. **73**, 2978-2981 (1994).

[30] D. Hochheiser, J. V. Moloney, and J. Lega, Controlling optical turbulence, Phys. Rev. A **55**, R4011-R4014 (1997).

[31] Polariton condensation in an optically induced two-dimensional potential, A. Askitopoulos, H. Ohadi, A. V. Kavokin, Z. Hatzopoulos, P. G. Savvidis, and P. G. Lagoudakis, Phys. Rev. B **88**, 041308 (2013).

[32] V. Ardizzone, P. Lewandowski, M. H. Luk, Y. C. Tse, N. H. Kwong, A. Lucke, M. Abbarchi, E. Baudin, E. Galopin, J. Bloch, A. Lemaitre, P. T. Leung, P. Roussignol, R. Binder, J. Tignon, and S. Schumacher, Formation and control of Turing patterns in a coherent quantum fluid, Sci. Rep. 3, 3016 (2013).

[33] J. Schachenmayer, C. Genes, E. Tignone, and G. Pupillo, Cavity-enhanced transport of excitons, Phys. Rev. Lett. **114**, 196403 (2015).

[34] V. Shahnazaryan, O. Kyriienko,and I. A. Shelykh, Adiabatic preparation of a cold exciton condensate, Phys. Rev. B **91**, 085302 (2015).

[35] N. Bobrovska and M. Matuszewski, Adiabatic approximation and fluctuations in exciton-polariton condensates, Phys. Rev. B 92, 035311 (2015).

[36] L. A. Lugiato and R. Lefever, Spatial dissipative structures in passive optical systems, Phys. Rev. Lett. **58**, 2209-2211 (1987).

[37] A. C. Newell and J. V. Moloney, *Nonlinear Optics* (Addison-Wesley: Reading, MA, 1992).

[38] J. Lega, J. V. Moloney, and A. C. Newell, Swift-Hohenberg equation for lasers, Phys. Rev. Lett. **73**, 2978-2981 (1994).

[39] J. Yang, *Nonlinear Waves in Integrable and Nonintegrable Systems* (SIAM: Philadelphia, 2010).

[40] V. Dunjko, V. Lorent, and M. Olshanii, Bosons in cigar-shaped traps: Thomas-Fermi regime, Tonks-Girardeau regime, and in between, Phys. Rev. Lett. **86**, 5413-5416 (2001).

[41] V. Skarka, N. B. Aleksić, H. Leblond, B. A. Malomed, and D. Mihalache, Varieties of stable vortical solitons in Ginzburg-Landau media with radially inhomogeneous losses, Phys. Rev. Lett. **105**, 213901 (2010).

[42] V. Skarka, N. B. Aleksić, M. Lekić, B. N. Aleksić, B. A. Malomed, D. Mihalache, and H. Leblond, Formation of complex two-dimensional dissipative solitons via spontaneous symmetry breaking, Phys. Rev. A **90**, 023845 (2014).